UNIVERSITÀ DI PARMA
ARCHIVIO DELLA RICERCA

University of Parma Research Repository

On the interaction between partially-reflected waves and an opposing wind

note finali coverpage

(Article begins on next page)

13 January 2025

On the interaction between partially-reflected waves and an opposing wind

F. Addona[a], L. Chiapponi[a], M. Clavero[b], M. A. Losada[b], S. Longo[a]

[a]*Department of Engineering and Architecture (DIA), Parco Area delle Scienze, 181/A, Università degli Studi di Parma, 43124 Parma, Italy*
[b]*Instituto Interuniversitario de Investigación del Sistema Tierra, Universidad de Granada, Avda. del Mediterráneo s/n, 18006 Granada, Spain*

Abstract

Air-sea interaction is a relevant topic with still many open questions, also in consideration of the numerous and complex scenarios that occur in nature. In this manuscript we report an experimental study of partially-reflected regular (long) waves under the action of an opposite wind, which generates short wind-waves (wind generated water waves, WGW). Wind blows against the incident wave, and therefore it is in the same direction as the reflected wave. Regular waves are generated by a paddle and are defined as mechanically generated water waves (MGW). MGW and WGW are separated by a spectral filtering technique, and free surface statistics of wave height, period and steepness are studied. The spatial variation induced by partial reflection of MGW (generated by paddles) is experimentally observed and theoretically described, and the effects of wind on reflection parameters are observed and examined. A phase-conditional analysis of wind-waves statistics, separating crest and through, and upwind and downwind, reveals the importance of the local wind forcing, and captures features of the wind-waves modulated by the longer waves which are not detected with standard statistical analyses. The phase celerity of the wind-waves is analysed including the effects of the wind-induced shear current and the non-inertial effects of the MGW; to the best of our knowledge, this last effect analysis is novel.

The study is relevant to characterize the wave field in front of coastal structures and beaches under wind and wind waves (co-linear in the same, and in the opposite direction) conditions, affecting run-up, overtopping and mean quantities modulated by the dynamic of group of waves.

Keywords: partial reflection, wind-waves and swell, phase celerity

1

1. Introduction

In many practical situations wind waves and swell coexist, with a variety of interactions and combinations due to different directions, presence of currents, of breaking, variable depth, reflection. The results available in the literature indicate that, in general, swell grows when ruffled by following wind, while the wind-generated waves and their growth are attenuated or suppressed when superimposed to longer waves (Belcher et al., 1994; Chen and Belcher, 2000). However, the results often differ by orders of magnitude and also predict different directions of momentum and mass transfer.

A shortcoming of the available studies is that they do not include wave reflection, although in coastal areas reflection (almost ubiquitously a partial reflection) of swell is always present and combines with a local wind action. Partial reflection is also relevant for bottom forms evolution, where several length scales coexist, with bar and ripples organized according to reflective conditions (Cobos et al., 2017). Several length scales are modified in the fluid domain as a consequence of reflection, and new length scales arise due to currents, to breaking, with eddies of different size acting together during the wave cycle (Longo, 2003; Clavero et al., 2016).

Some research works (Peirson et al., 2003; Stewart and Teague, 1980) revealed inconsistencies in the experimental results attributed to the effects of reflective conditions, even though they did not include a systematic analysis of these effects. Olfateh et al. (2017) showed that wave Reynolds shear stress, responsible of momentum transfer between air and water, can be prominent in the wave field when a reflected wave component is present also in little percentages (5-10%, a typical value for a dissipative beach), although they did not consider the phase shift between the incident and the reflected waves. Addona et al. (2018) carried out experiments of mechanically generated waves (MGW) plus following wind with an active absorption system, covering a wide range of reflective conditions. They derived a theoretical model for the wave field, including the phase shift of the MGW, the presence of a bound wave and linearly intersecting waves. Such a model can be solved obtaining the free surface level and the velocity components, from which the wave Reynolds stresses can be easily calculated. The role of both the reflection coefficient and phase shift on the spatial modulation of the wave field was highlighted. It was also observed that the wave Reynolds shear

stress, in the presence of reflection can be in some circumstances an order of magnitude greater than the turbulent Reynolds shear stress induced by the wind. Further complications arise in the presence of currents interacting with wind-wave generation Chiapponi et al. (2020).

Combined seas are a relevant problem in open ocean, where they are responsible for several ship accidents (Toffoli et al., 2005), and nearshore, where the reflected swell generates a very complex environment. Many researchers have been working on the interaction between near-following and crossing seas (Toffoli et al., 2008, 2011; Bitner-Gregersen and Toffoli, 2014). In particular, combined sea states with wind sea and swell, enhance the frequency occurrence of rogue waves for sea states crossing at an angle of $40° - 60°$ (Bitner-Gregersen and Toffoli, 2014). To the best of our knowledge, a detailed analysis of wind-waves in the presence of swell and partial reflection has not been yet performed, presumably as a consequence of the difficulties in changing the reflection coefficient during the experiments. With the aim of filling this gap, in this work we present the experimental results of monochromatic paddle-generated waves (MGW) under the action of an opposing wind, for different reflective conditions. We investigate the kinematic of the composite wave field, with a separation of the two components (MGW and wind-generated waves, WGW) through a spectral filter, with a focus on the WGW as affected by the presence of MGW.

In order to clarify the terminology, we remind that we define MGW the waves generated by a paddle, and WGW the waves generated by the wind due to a fan blowing in the wind tunnel covering the flume. In the present experiments the former are regular periodic and are much longer than the latter, and reproduce a swell; WGW are also named short waves and are randomly distributed. The experiments are conducted in a flume and the waves have no average directional spreading. Indeed the crests of the WGW have a directional spreading since are short waves even at the small scale of the flume width, but are reflected by the walls, creating a pattern which, as a first approximation, can be considered periodic in the transverse direction, and with an average propagation along the axis of the flume. The short waves pattern, only in "average" colinear with the channel axis, is an aspect that will require proper analysis in future experiments.

The paper is structured as follows. In §2, the experimental set-up and protocol are illustrated, including some details on data processing. The MGW component is studied in §3, where also the influence of the wind on the re-

flection parameters is documented. The statistics of the wind-waves, along with the phase-conditional analysis are reported in §4, while the analysis of the wave phase and group celerities is reported in §5. The discussion of the results and the conclusions are summarized in §6.

2. Experiments

2.1. The experimental facility and the instruments

The experimental activity was conducted in the Ocean-Atmosphere Interaction flume (CIAO) located in Granada, Spain (see Addona, 2019, for details). The flume, with length 16 m, width 1.0 m and height $\approx$ 2 m (0.70 m is the still water depth), allows the generation and coupling of current, mechanically(paddle)-generated waves, wind generated waves and rain. The CIAO can recreate different reflective conditions for regular and irregular waves, thanks to a PC-controlled active system for wave generation/absorption based on two paddles on opposite sides of the flume. The active absorption system uses real-time measurements of the water level at the paddles in order to obtain a desired reflective condition of regular and irregular waves. In these experiments, the wave is generated by paddle No 2 and it propagates towards paddle No 1. Paddle No 1 movement can be programmed to completely reflect the incoming wave (perfect reflection condition), to absorb the incoming wave and to partially reflect the incoming wave on the base of a specific transfer function. This, in turn, is equivalent to mimick a desired reflective condition inside the flume. Paddle No 2 generates the initial wave and compensates the effects of the re-reflected waves, which would propagate from paddle No 2 to paddle No 1. We refer to Lykke-Andersen et al. (2016) for more details on the transfer function (and the filtering methods) which controls the CIAO reflective conditions of regular (and irregular) waves. The present activity is focussed on WGW superimposed to MGW propagating from the opposite direction (the mix of waves is named as mechanical plus wind generated water waves, MWGW), and the analysis is devoted to the kinematics of the composite waves in the flume.

The displacement of the water surface was measured with eight UltraLab ULS 80D (US) ultrasonic probes with a nominal accuracy of 0.3 mm and a data rate of 75 Hz. According to the manufacturer specifications and taking into account the geometry of the installation, the beam footprint diameter is $\approx$ 20 mm. Since the wavelength of the WGW varies between 0.4 and 0.7 m (see figure 13), the footprint represents $\approx 1/35 - 1/20$ of the wavelength,
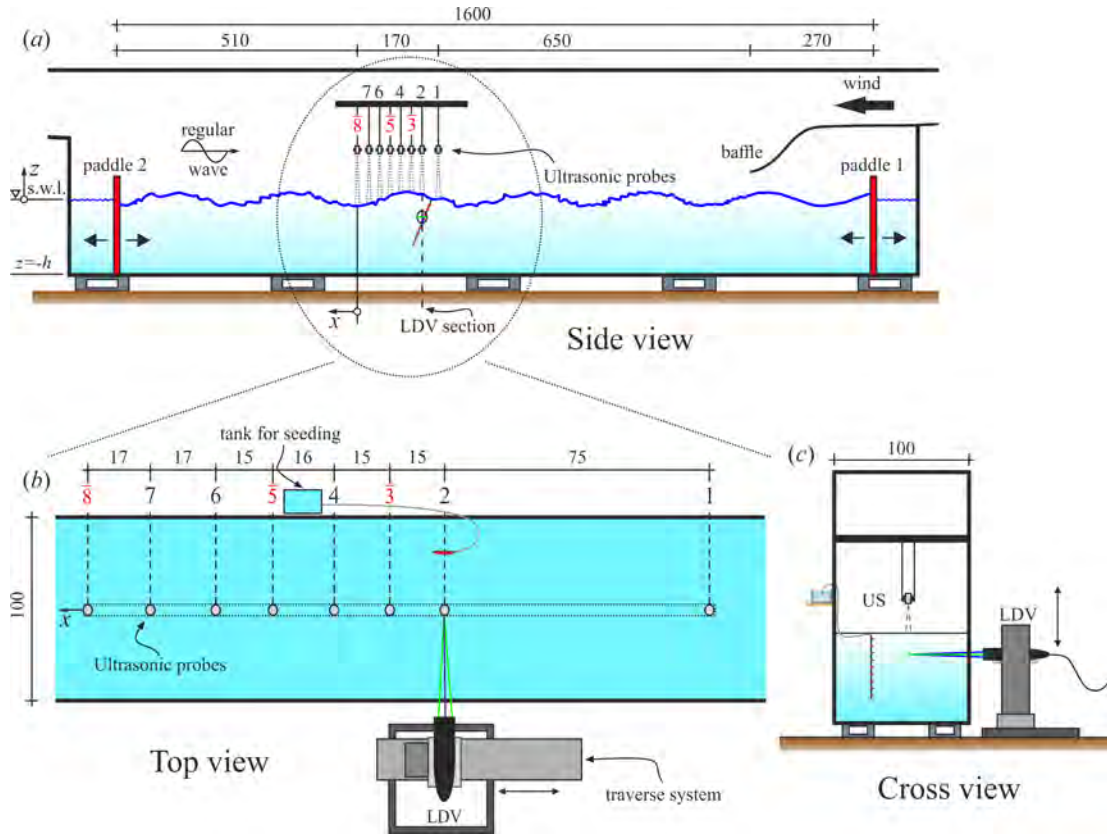
4

Figure 1: The experimental flume and schematic of the probes. *a*) Side view of the flume, *b*) top view, *c*) cross view. Sizes are in centimetres. The Ultrasonic Probes at sections 8, 5 and 3 were used for reflection analysis.

with a resolution comparable to the overall accuracy in the evaluation of the phase celerity (see §5). More details about the celerity uncertainty derived from US measurements are given in Chiapponi et al. (2020) (their subsection 3.3). The fluid velocity in water was measured with a Doppler Velocimetry (LDV) laser technique in a single section and approximately in the mid-plane of the flume, and the velocity of the air was measured with a Pitot tube. A sketch of the experimental set-up is shown in figure 1.

2.2. Scaling

The correct scaling between laboratory (the model) and field (the prototype) data in wave flumes, requires the analysis of the similarity laws. The

problem is well known and, although its principles are simple, the criteria for developing similarity are quite tricky for complex experiments involving airflow and wave motion. For the water, the physical process we are analysing can be described in terms of nine variables: a velocity scale, a length scale, time, density, viscosity and tension surface of the fluid, pressure, fluid bulk compressibility and gravity acceleration. A group of three of the variables are independent and, by mean of Buckingham's theorem, the problem can be formulated as a function of six non dimensional groups, namely Reynolds, Froude, Weber, Strouhal, Euler, Mach numbers (see, e.g., Massey, 1971; Hughes, 1993). The governed variables are the wave height and period, the wave length, the characteristics of the spectrum, etc., which become dimensionless upon the appropriate scaling with the fundamental quantities. The similarity requires an equal value of each of these groups in the model and in the prototype, hence three degrees of freedom are left. However, by using water in the laboratory experiments and in the presence of gravity acceleration, five constraints are added, since viscosity, density, tension surface, bulk compressibility have the same values in the model and in the prototype, and the complete dynamic similarity is not allowed. A partial similarity is achieved by neglecting the Reynolds number in the hypothesis that it has minor effects (especially in the air boundary layer), neglecting the Weber number in the hypothesis that the curvature of the air-water interface is limited, neglecting the Mach number in the hypothesis that compressibility of the water (water is often mixed with air bubbles) is not relevant (it is assumed that aerated breaking or very fast movement of the breakers, conditions in which a transonic state may locally exist (see Peregrine, 2003), do not occur in the field, so reproduction of these effects in the laboratory is not required). In these conditions a Froude similarity can be adopted, with length and pressure scales equal to λ, a velocity and a time scales equal to $\sqrt{\lambda}$. Strouhal and Euler similarities are also satisfied. Since Reynolds, Weber and the Mach number similarities are not exactly fulfilled (the ratio between the values in the model and in the prototype is $r_{Re} = \lambda^{3/2}$, $r_{We} = \lambda^2$ and $r_{Ma} = \lambda^{1/2}$ for the Reynolds, the Weber and the Mach number, respectively), some scale effects are expected in transforming the experimental measurements in the laboratory into field values, with a larger distortion for decreasing length scale ratio λ: a reduced Reynolds number could bring to less effective transport of momentum in the model than in the prototype (see Chiapponi et al., 2020, for details on the Reynolds number variability); a reduced Weber number increases the role of tension surface effects in the

model, with a reduction of air inclusion; a reduced Mach number hides possible shock effects (see, e.g. Peregrine, 2003; Bredmose et al., 2015). For the air flow we have a velocity scale, a length scale, time, density, viscosity, pressure. We are interested in the boundary layer above water, neglecting large scale pressure and velocity pulsations which are present in a real wind blowing over the sea, neglecting also air compressibility since real wind flow is isochoric. As far as time scales are concerned, there are a number of them mainly related to turbulence, and a very relevant one is the period of fluctuating pressure, considered quite important in wave growth (Teixeira and Belcher, 2006). In the early stage of wave generation, a time scale related to the shear rate in the air boundary layer is considered relevant. Toba (1988) reported a picture where both the air and the water layers have a structure which is similar to that of the turbulent boundary layer over a rough solid wall, hence the classical scales of boundary layers are chosen: friction velocity, apparent roughness of the surface, mass density and viscosity, and a time scale varying during process. Three convenient dimensionless groups are Reynolds number $Re_a = u_{*,a} z_0 / \nu_a$, Euler number $Eu_a = \Delta p / (\rho_a u_{*,a}^2)$, a Strohual number $St_a = z_0 / (u_{*,a} t)$, where the subscript "a" refers the variable to the air. Assuming the same Froude scaling used for the water side process, Euler and Strohual similarity in the ear side are satisfied, Reynolds is not, since $r_{Re_a} = \lambda^{3/2}$: if the length scale is too small, the regime of the air boundary layer in the laboratory can be transitional although it is turbulent or fully turbulent in the field.

Bearing in mind the limits of the laboratory experiments with respect to the field process, we assume that the numerous uncertainties on the characteristics of the waves and of the wind, on reflection conditions in the field (close to the coast), and on all the other parameters and variables, by far outweigh the scale effects uncertainties, which can be confidently neglected.

2.3. Protocol of the tests

Five experiments were performed, with the same nominal MGW characteristics and with a constant opposing-wind speed, and with different reflective conditions, as listed in table 1. Given the complexity of the present experiments, it is appropriate to provide more details on the development of the experimental wave field in the channel. The regular MGWs propagate in the opposite direction to the wind acting on the free surface. As described above, the active absorption system allows the reflection coefficient of the

Expt	$u_{*,a}$ $(\mathrm{cm\,s^{-1}})$	H_i (cm)	T (s)	K_r	$\Delta\varphi$ (rad)
PoW1	75.2	4.8 ± 0.1	1.6	0.843 ± 0.003	4.33 ± 0.03
2	75.2	5.3 ± 0.1	1.6	0.658 ± 0.004	4.38 ± 0.03
3	75.2	5.8 ± 0.1	1.6	0.337 ± 0.007	4.54 ± 0.04
4	75.2	5.5 ± 0.1	1.6	0.132 ± 0.010	5.01 ± 0.06
5	75.2	5.4 ± 0.1	1.6	0.099 ± 0.006	0.15 ± 0.17

Table 1: Parameters of the five experiments with "MGW with an opposing Wind"(PoW), having a constant nominal incident wave height and period and in the presence of a constant wind speed, but with different reflective conditions. $u_{*,a}$ is the air friction velocity, H_i is the estimated incident wave height, T is the MGW period, K_r and $\Delta\varphi$ are the reflection coefficient and the phase shift, respectively. The uncertainty equals one standard deviation.

regular wave to be controlled. Therefore, a specific reflection condition appears as a consequence of a software controlling in feed-back the movement of the two paddles. In other words, the reflection coefficient results from the combined action of the two paddles. In reality, we are not interested in what is the physical source of the reflected waves, and we have a complete description of the reflection given by the reflection coefficient and the phase shift. In addition, the presence of wind generates an even more complex environment. In fact, the wind modifies the reflection conditions by attenuating the reflection coefficient and also influencing the phase shift, as described in the following.

The air friction velocity $u_{*,a}$ derives from the interpolation of the log-law $U/u_{*,a} = 1/k \log(z/z_0)$, where U is the air velocity, $k = 0.4$ is the von Kármán constant and z_0 is the roughness length. In order to clearly detect the effects of wind on the flow field, in particular on reflection, before starting the fan five minutes of MGW only were generated measuring the water surface displacement. Each experiment lasted ≈ 300 s (MGW only) plus 3600 s (for MWGW). Figure 2 shows a sequence of snapshots for one of the experiments, showing the short waves riding the long wave.

Free surface data were acquired with MGW only and with MWGW. Phase averaging of the free surface was performed in both conditions to compare the results and to identify the effects of the wind on the periodic long wave
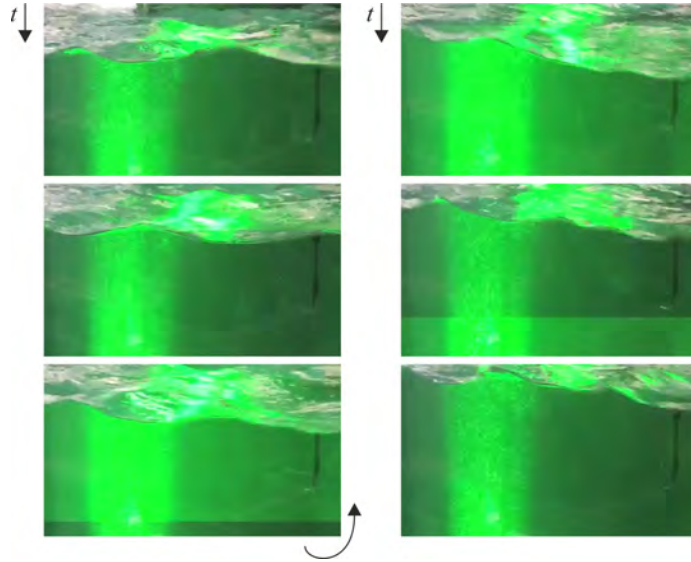
8

Figure 2: Snapshots of an experiment, with time interval between two frames equal to 0.13 s. The light is due to a laser sheet for PIV measurements, not included in the present analysis.

shape. The uncertainties related to the experimental values are calculated on the ensemble averages of sub-samples of the signal, the confidence intervals of the theoretical relations are evaluated through a Montecarlo simulation by assuming a normal distribution of the reflection parameters K_r, $\Delta\varphi$, and of the incident wave H_i.

2.4. Data analysis

The reflection analysis is based on three gauges surface level measurements (Mansard and Funke, 1980), with the least square model detailed in Baquerizo (1995). Such analysis measures the reflected waves from paddle No 1, and it allows the estimation of the incident wave height H_i, the reflection coefficient K_r and the phase shift $\Delta\varphi = \varphi_i - \varphi_r$ of the reflected wave. We remind that the phase shift indicates the position of quasi-nodes and quasi-antinodes and determines the spatial variation of the MGW. Hence, all the reflection analysis could be misleading without an adequate evaluation of this parameter. H_t is the total wave height, a local variable representing the maximum excursion of the water level at a given section of the flume.

Figure 3 shows the phase-averaged wave profile for experiments PoW1-5 at different sections; for clarity, only data from sensors US1-3-5-8 are reported

and the initial phase is shifted to zero. In the absence of wind, the wave shape is regular with very little deviations from regularity. In the presence of opposing wind, the wave profile shows larger deviations of the order of the wind-waves height. For low reflection, the wave shape is slightly different from the periodic MGW and is almost homogeneous along the flume, while it is modulated in amplitude for increasing reflection coefficients K_r, and is distorted. The distortion is attributed to non linear interaction between wind waves and MGW. The balance is amongst energy influx due to the wind, energy flow due to the MGW, energy dissipation and energy transfer due to breaking. Feddersen and Veron (2005) found that for shoaling waves in the laboratory, the wind action moves the breaking point and breaking height as a consequence of nonlinear interaction with shoaling. They also found that co-flowing wind modifies the skewness and the asymmetry.
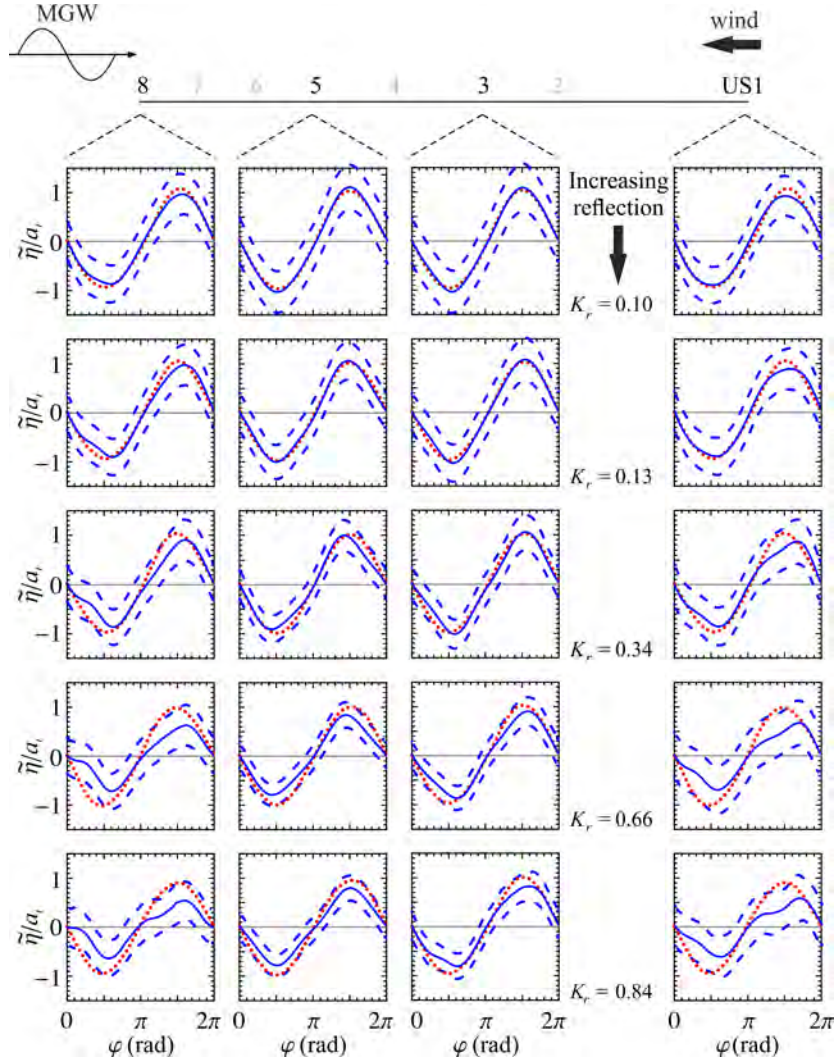
Figure 3: Phase-averaged wave profiles $\widetilde{\eta}$ for different reflective conditions, non-dimensional with respect to the local wave amplitude a_t of the MGW only. Red dotted lines refer to MGW only, blue solid lines refer to MWGW, dashed lines are one standard deviation for MWGW. Fetch increases from US1 to US8. For an easy visualization, only signals from sensors US1-3-5-8 are shown.

The Fast Fourier Transform of US data has been applied to elaborate the spectrum of the signal in the frequency domain. The periodic component (MGW) is obtained by filtering the spectrum in the frequency band $0.5 < f/f_{peak} < 1.5$, where f_{peak} is the peak frequency, while the non-periodic component (WGW) is obtained by high-pass filtering with a threshold of $f/f_{peak} > 2.2$ (to avoid the contamination of the second-order harmonic). The energy not included after filtering MGW and WGW frequency bands is at most 4% of the total energy, which is considered negligible.

Figure 4 shows the power spectral density (PSD) in section 8 for different reflective conditions, with the shaded areas representing the windows used to extract the long-wave (band-pass filtering) and the short-waves (high-pass filtering). The spectra in the other sections (not shown) are similar, with variations due to the space modulation of the long-wave component in the presence of reflection, and due to different fetch length.

The energy partition between the different wave components indicates that the MGW is generally dominant, with the energy input from the wind progressively increasing in the presence of the maximum reflection.
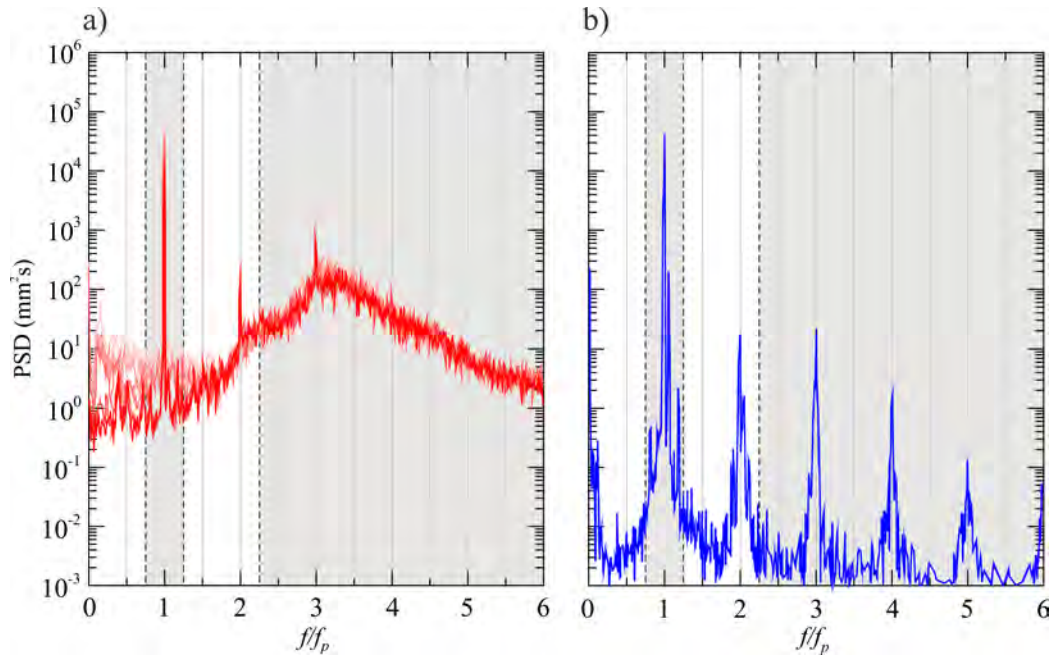
Figure 4: Power Spectral density (PSD) of free surface elevation at section 8 for five experiments with increasing reflection coefficient. a) MWGW, the intensity of the color is proportional to the reflection coefficient (i.e., the darker the color, the higher the reflection coefficient); b) MGW only as recorded for 300 s before switching on the fan. The shaded areas indicate the windows used for filtering the MGW (the left one across the main peak) and the WGW (the right one, after the second harmonic peak of the MGW component).

3. Paddle-waves

The total wave amplitude a_t is measured (i) with MGW only (in the absence of wind), and (ii) with MWGW. The MGW component contribution to the instantaneous free surface level is obtained filtering with a band-pass filter the spectrum of the experimental US signal as detailed in §2. The first order theoretical free surface level of a partially-reflected regular wave (see equation 8 in Addona et al., 2018) is:

$$\widetilde{\eta}(x,t) = a_i[\cos(kx - \omega t + \varphi_i) + K_r \cos(kx + \omega t - \varphi_r)], \tag{1}$$

where $a_i = H_i/2$ is the incident wave amplitude, K_r the reflection coefficient and φ_i, φ_r the phase of the incident and the reflected waves, respectively. The values of the reflection parameters, K_r and φ_i, φ_r, are evaluated from the reflection analysis described in §3.

Figure 5 shows the experimental and theoretical wave amplitude for MGW only and for MWGW, as a function of x/L, where the wave length L is calculated from linear dispersion relation. We observe a good agreement between theory and experiments, with the modulation of the wave amplitude due to reflection along the flume also for small values of K_r and $\Delta\varphi$. In the presence of opposite wind, we observe an attenuation of the wave height and a shift of nodes and anti-nodes in the opposite direction of the wind, with respect to the MGW only. The theoretical curves overestimate the experimental values for all the tests, with deviation $\leq 5\%$ of the total wave amplitude, which is attributed to the wind-induced dissipation not included in eq.(1). This result suggests that (i) the dissipations due to the wind is small but not negligible in limited fetch conditions, (ii) the MGW travels with a wave shape and celerity slightly modified by the wind action.

The spatial variation of the mean water level under reflective conditions can be predicted using theory; for example, Addona et al. (2018) developed a model based on the radiation stress concept. However, the role of reflection has often been neglected, and we are not aware of previous works showing the relfective conditions as the main cause of the spatial variation. It is also relevant to notice that the spatial variation does not only depend on the reflection coefficient K_r, but also on the phase shift $\Delta\varphi$.

From the model by Addona et al. (2018) (their equation 16), the theoretical mean water level at the first order reads

$$\bar{\eta} = k a_i^2 K_r \coth 2kh \cos(2kx + \Delta\varphi) + \text{const}, \tag{2}$$
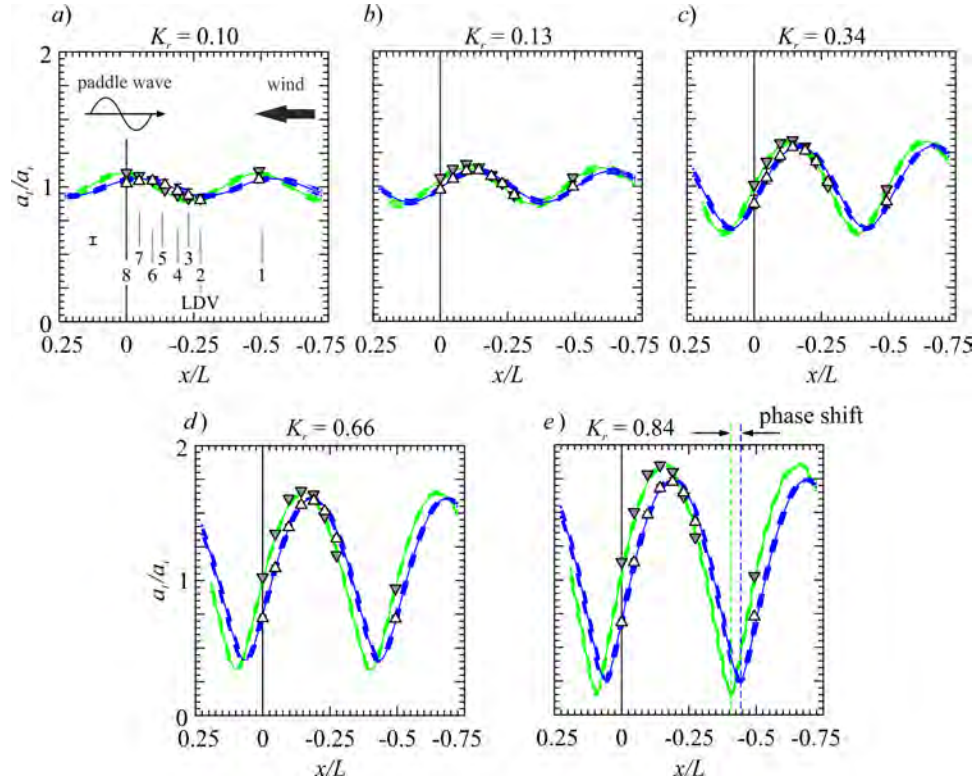
14

Figure 5: Spatial modulation of the measured wave amplitude a_t/a_i, for different reflective conditions. Green lines are theoretical MGW, blue lines are theoretical MWGW, filled triangles refer to experiments without wind (MGW only), empty triangles refer to experiments with MWGW. Dashed lines are the 95% confidence limits, the error bars are two standard deviations. The numbers in panel a) are in the section of the US probes, with LDV measurements in section 2; the vertical dashed lines in panel e) indicate the phase shift $\approx \pi/8$ of the envelopes of MGW and MWGW.
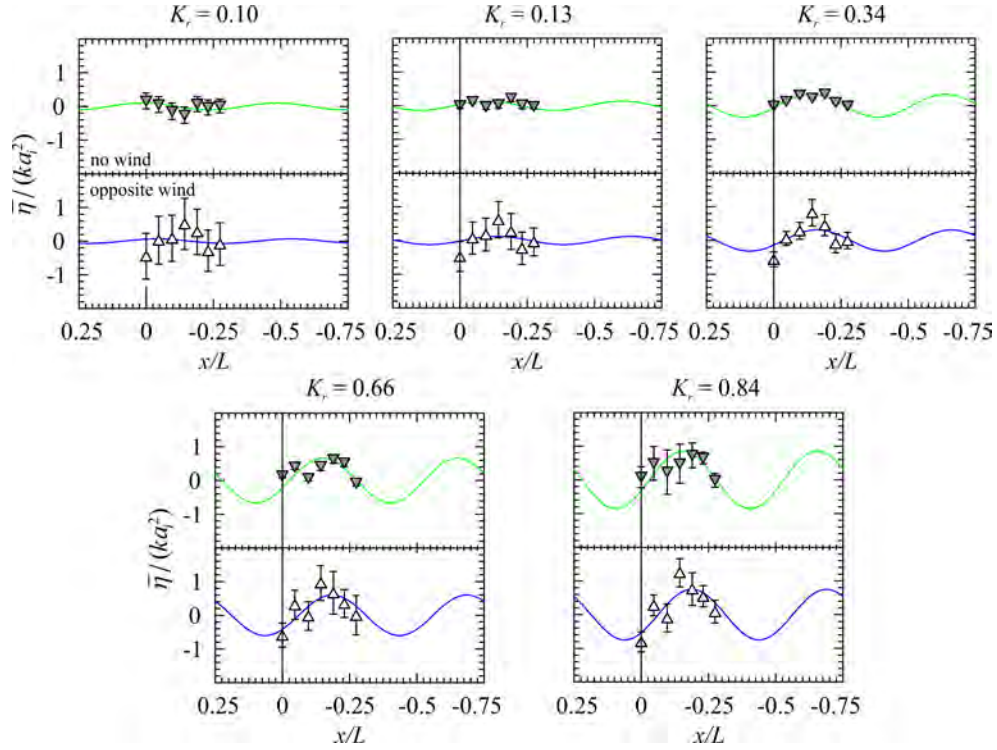
Figure 6: Mean water level for different reflective conditions, MGW only and MWGW. Lines are theory from eq.(2), symbols are experimental values. Error bars are two standard deviations.

where the constant is imposed by mass conservation. Figure 6 shows the comparison between the theoretical and the experimental mean water level, with a spatial modulation induced by reflection again evident and with results in a good agreement with theory.

Overall, the technique adopted for separating MGW and WGW gives results which reproduce correctly the theoretical models of the spatial amplitude and mean water level derived for regular components only. The technique can be confidently assumed as reliable.

Figure 7 shows the variations of the incident wave height H_i, the reflection coefficient K_r and the phase shift $\Delta\varphi$ in the presence or absence of opposite wind. The values are listed in Table 2. The presence of opposing wind induces (i) an attenuation of the height of the incident wave $H_{i,w}$, larger for a higher reflection coefficient; (ii) a reduction of the reflection coefficient

16

Expt	$(H_{i,w} - H_i)/H_i$	$K_{r,w} - K_r$	$\Delta\varphi_w - \Delta\varphi$
PoW1	-0.212 ± 0.003	-0.099 ± 0.003	-0.42 ± 0.03
2	-0.179 ± 0.002	-0.063 ± 0.004	-0.43 ± 0.03
3	-0.070 ± 0.001	-0.031 ± 0.009	-0.33 ± 0.04
4	-0.021 ± 0.003	-0.012 ± 0.01	-0.44 ± 0.05
5	-0.024 ± 0.004	-0.033 ± 0.006	-0.65 ± 0.14

Table 2: Variation of the reflection parameters for MWGW (subscript "w") and MGW (no subscript). H_i is the incident wave height, K_r is the reflection coefficient and $\Delta\varphi$ is the phase shift between the incident and the reflected waves. Reflection decreases from Expt PoW1 to Expt PoW5.

$K_{r,w}$, more pronounced for a larger K_r; (iii) a negative shift of the phase lag $\Delta\varphi_w - \Delta\varphi$, with a reduction $\approx -\pi/8$ rad almost independent of K_r except at low reflection coefficient. Also wind driven currents are generated and their effects will be discussed in §5. The physical interpretation of these effects is by far not simple and these results give more and new insights about the non-trivial interaction between wind and waves under reflective conditions. Further work and experiments are required to reach firm conclusions.

We need to analyse the source of the wave attenuation, in order to understand if it is due to the attenuation rate generated by opposing wind or is the consequence of a reduction of the reflection coefficient. According to the model by Peirson et al. (2003), applying their eq.(11) results that in the fetch of our measurements (the distance between US2 and US8, which is $\approx 1\,\mathrm{m}$) the maximum dissipation is $1 - E_{\mathrm{US2}}/E_{\mathrm{US8}} \approx 7.4\%$ of the total energy, equivalent to a free surface elevation attenuation $\approx 2.7\%$. This value is consistent with values for experiments with low reflection coefficient (Expts 4-5), but it is much smaller than values measured in the experiments with high reflection coefficient (Expts 1-3), hence other phenomena should be invoked. Indeed the wave profiles shown in figure 3 give evidence of the role of wind action in reshaping the regular waves, with super harmonics of increasing energy describing a non-linear wave. We guess that non linearity induced by WGW superimposed to MGW may have a role in the attenuation of the incident wave and in the reduction of the reflection coefficient, but further experiments are necessary to shed light on the phenomenon.
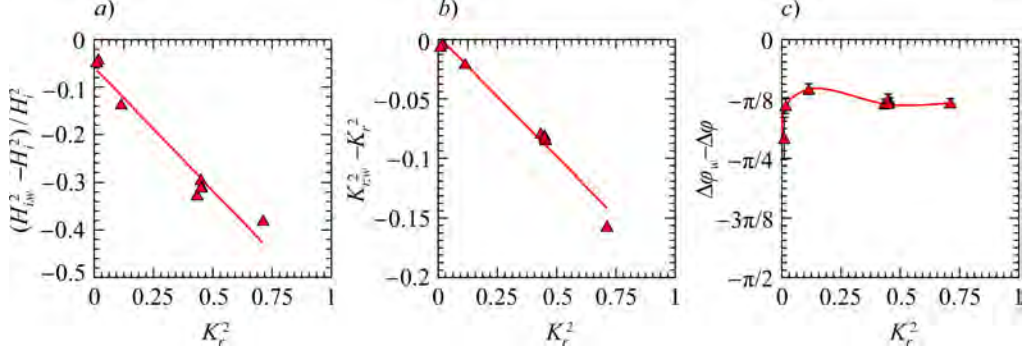
Figure 7: The influence of an opposing wind on the reflection parameters as a function of the reflection coefficient. *a*) Attenuation of the non-dimensional incident wave height $\left(H_{i,w}^2 - H_i^2 \right)/H_i^2$; *b*) reduction of the squared reflection coefficient $K_{r,w}^2 - K_r^2$; *c*) variation of the phase shift $\Delta\varphi_w - \Delta\varphi$. Subscript "*w*" indicates the presence of wind, no subscript indicates no wind. Symbols are the experimental data, interpolated by solid lines. Error bars are two standard deviations.

4. Wind-waves

A zero–crossing analysis was performed for the WGW (i) considering the whole sample, and (ii) applying a phase-conditional analysis to separate the WGW according to their position with respect to the phase of the MGW. Figure 8a shows H_{rms} and the wave steepness kH_{rms}, figure 8b shows the mean T_m as a function of the non-dimensional fetch length. The scales are $g^{-1}u_{*,a}^2$ and $g^{-1}u_{*,a}$ for the length and the time, respectively, where $u_{*,a}$ is the air friction velocity. The two dashed lines are representative of the most common wave generation models, with the exponent of the fetch length about 0.5, for the wave height, and about 0.33 for the wave period.

For all the experiments an initial growth of WGW is followed by an attenuation, where micro-breaking dissipates energy and transfer energy to longer waves. The generation plus dissipation term depends on reflective conditions, with smaller growth rate for higher reflection: the WGW height H_{rms} at $K_r = 0.84$ is reduced $\approx 10\%$ with respect to H_{rms} at $K_r = 0.10$. The WGW period growth rate shows a reduced variability with the reflection coefficient, without a clear-cut trend.

The ratio between the WGW height and the total wave height, H_{rms}/H_t is in the range $0.5 - 1.1$ for US2 and US8, and varies between $0.4 - 0.7$ for the other sections of measurement, while the ratio of the WGW to the
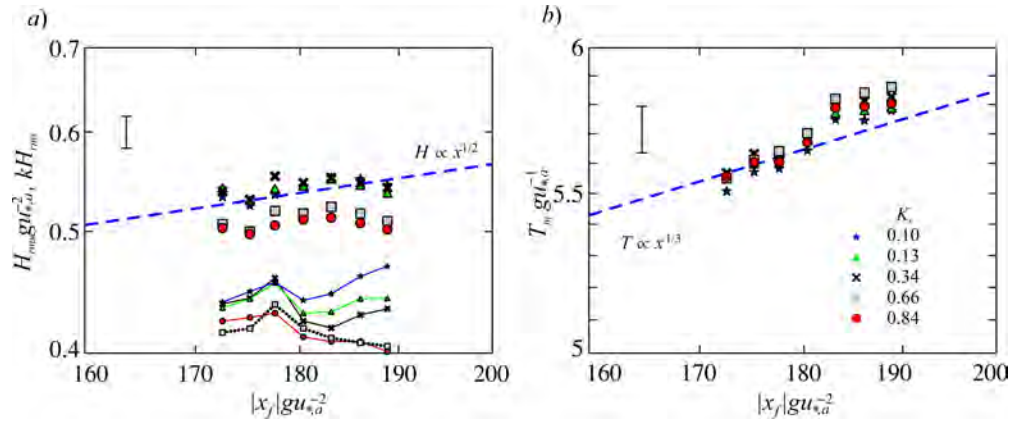
18

Figure 8: Fetch variation of the WGW statistics. a) The root mean square height H_{rms} (symbols) and the wave steepness kH_{rms} (lines plus symbols) as a function of the fetch length x_f, non-dimensional with the length scale $u_{*,a}^2/g$. b) The mean period T_m (symbols) as a function of the fetch length x_f non-dimensional with the time scale $u_{*,a}/g$. The dashed lines represent a theoretical trend for limiting fetch, symbols represent experiments and error bars are one standard deviation.

MGW length is in the range $0.11 - 0.14$. The variation of the ratio H_{rms}/H_t is mainly due to the spatial variability of the MGW total height H_t. The steepness is initially decreasing, then increases with a common maximum before collapsing, with a second growth ramp but only for $K_r < 0.34$.

It is known (Unna, 1947; Longuet-Higgins and Stewart, 1960; Phillips, 1963; Hasselmann, 1971) that short waves riding on longer waves have different wavelength and height according to their position, on the crest or on the trough of the longer waves. The wavy shape of the free surface suggested that the wind forcing has different effects when applied leewards or windward from the crest. Some laboratory experiments (Buckley and Veron, 2019) gave evidence of airflow separation past the wave crests, which justifies an asymmetric action of the wind. In order to detect the asymmetries, we performed a phase conditional analysis by classifying the WGW statistics on the basis of their position with respect to the MGW phase. We divided the MGW length into four sub-domains, namely a crest, a downwind side, a trough and an upwind side. This approach resembles the WKBJ approximation where the analysis develops by assuming that there are well different scales of the process, and that it is possible to average over these scales (length or time) separately: here we are assuming that the short waves properties can be con-

19

fidently averaged over a quarter of the long wave (length or period). After that, the entire process is analysed in terms of the averaged values.

Figure 9 shows the WGW height H_{rms} as a function of the fetch length, for different reflective conditions and in the four sub-domains upwind, downwind, crest and trough. The dashed lines are the interpolation for the minimum (blue dashed line) and the maximum (red dashed line) reflection coefficient.

For the minimum reflective conditions, $K_r = 0.10$, the WGW height grows with the fetch length in the four subdomains, with a growth factor almost null in the crest ($H_{rms} \propto x^0.09$) and $\propto 0.61$, 0.58 and 0.44 in the downwind, trough and upwind side, respectively. For the maximum reflective conditions, $K_r = 0.84$, WGW strongly decay in the downwind ($H_{rms} \propto x^{-1.60}$) and grow in the three remaining subdomains (0.64, 0.28 and 1.17), with maximum growth rate in the upwind.

The overall picture can be resembled by considering that wind waves are subject to input of energy by the wind but also to energy dissipation and to energy transfer to longer waves. Transfer of energy from short to long waves has been modelled by an interaction stress tensor and by a potential energy flux through mass transfer (see Hasselmann, 1971). A physical insight is obtained with a schematic where short waves riding long waves generate an oscillatory boundary layer near the free surface with displacement thickness modulated along the wavelength of the long wave: the varying thickness of the boundary layer works against the mean vertical velocity of the long wave, the shear stress works against the horizontal orbital velocity. In addition, the spatially varying thickness of the boundary layer requires an exchange of mass between the long and the short waves, with a net flux from the crest to the trough of the former, and this is equivalent to an energy loss of the long waves since potential energy per unit weight is higher at the crest than at the trough. For free propagating waves, the net balance between the energy transferred to the long waves by the short waves through interaction, and the energy loss due to the mass flux from the crest to the trough is null at the first order, and is negative at the second-order (Hasselmann, 1971). In the present experiments we are dealing with a flow field where incident and reflected components coexist and compose with different intensity depending on the value of K_r, generating quasi-nodes and quasi-antinodes, the former with a reduced vertical velocity amplitude, the latter with a reduced horizontal velocity amplitude. If we consider the model by Hasselmann (1971), the interaction stress works with space varying intensity against the fluid velocity, and with a different level of energy exchange according to the value of

20

the reflection coefficient. As a consequence, the energy balance of the waves (short and long waves) is affected (i) by the wind energy input; (ii) by dissipation; (iii) by spatially varying transfer according to the crest-trough position and according to the position with respect to the nodes/antinodes. We notice that in the present experiments the position of the nodes/antinodes as dictated by the phase shift in Figure 7c, does not change with K_r except for $K_r \rightarrow 0$.

It is also of interest to analyse the evolution of the WGW steepness kH_{rms} as shown in figure 10. For the minimum reflective conditions, the WGW steepness increases with the fetch length with a growth rate in the range 0.18–0.71; the maximum is reached at the downwind and the minimum at the crest. By increasing the reflective conditions to $K_r = 0.84$, the behaviour changes dramatically depending on the MGW phase: on the downwind, we observe a strong decay of the WGW steepness with $kH_{rms} \propto x^{-2.43}$, while in the trough and the crest $kH_{rms} \propto x^{-0.56}$ and 0.20, respectively; only in the upwind side we observe a positive growth rate with $kH_{rms} \propto x^{0.33}$.

In summary, the fetch evolution of the WGW is more complex than that obtained by phase averaging the results, much more sensitive to the MGW phase position if high reflecting conditions are present. It is also subject to the spatial modulation generated by reflection, with amplitude of the MGW and fluid velocity varying according to the position of the section with respect to the nodes and antinodes. Finally, it must be stated that present measurements have been performed just in the middle of the flume, without the possibility to completely track the growth of wind-waves as a function of fetch. In this respect, new experiments are required in order to extend the present dataset and to further support the present conclusions.
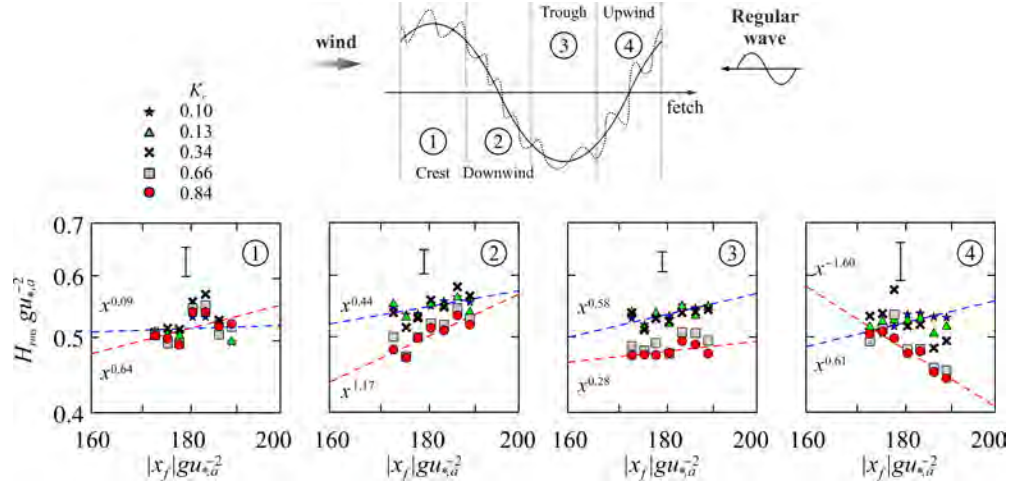
Figure 9: The WGW height $H_{rms}gu_{*,a}^{-2}$, as a function of the fetch $|x_f|gu_{*,a}^{-2}$, for different position of the MGW and for different reflection conditions. Symbols are the experiments, error bars are one standard deviation. Lines indicates a power interpolation for the lower reflective conditions (blue dashed, $K_r = 0.10$) and the higher reflective conditions (red dashed, $K_r = 0.84$).
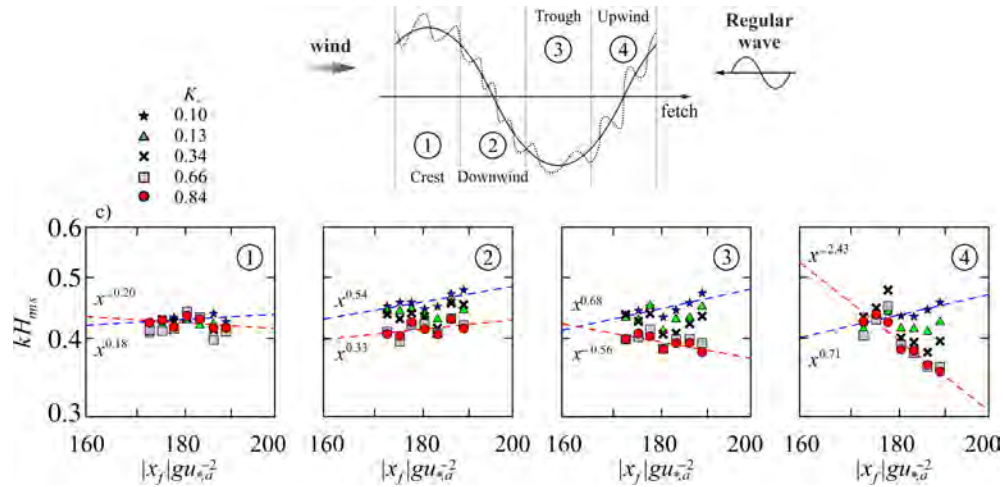

Figure 10: The WGW steepness kH_{rms}, as a function of the fetch $|x_f|gu_{*,a}^{-2}$. For caption see figure 9.

5. Phase and group celerities

The separation of the periodic MGW and the fluctuating WGW components is based on the linear spectrum of the free surface elevation and implicitly assumes that WGW are linearly combined with the MGW and propagate with their own phase celerity. In this sense, we neglect non-linear direct interactions between the regular MGW and the WGW. This approximation has been verified as acceptable for the prediction of the spatial variation of the amplitude and of the mean water level, and is generally accompanied by a significant spectral separation of the WGW and the MGW. In the present experiments the wavelength of the MGW is ≈ 3.4 m and the average wavelength of the WGW is ≈ 0.5 m, which results sufficient to justify the linear approach.

With the same approach, the phase celerity of the WGW is computed by assuming that WGW move with the peak frequency of the spectrum after removal the main peak due to the periodic component. However, the linear dispersion relation $\omega^2 = gk \tanh kh$, where ω is the angular peak frequency of the WGW, g is the gravitational acceleration, k is the WGW wave number and h is the water depth, requires a correction to include the non-linear effects of sheared currents emerging in the presence of a wind. The correction is based on the model by Swan and James (2000):

$$c = \sqrt{\frac{g}{k} \tanh(kh)} + D + c_1, \tag{3}$$

where D is a shift of the phase celerity due to the wind drift at the air-water interface, and

$$c_1 = -\frac{C}{2k} \tanh(kh) + \frac{B}{2k^2} - \frac{3A}{4k^3} \tanh(kh) - \frac{C}{4k \tanh(kh)} \operatorname{sech}^2(kh), \tag{4}$$

is a second-order correction due to non-linear interactions between waves and current. A, B and C are three of the four coefficients of a third order polynomial approximating the current velocity profile:

$$\bar{u}(z) = Az^3 + Bz^2 + Cz + D. \tag{5}$$

Eq.(3) is based on perturbation methods in the small parameter $\epsilon = ka$, being a the amplitude of the waves (in the present experiments $O(ka) \approx 10^{-1}$), and is valid for all profiles of weak currents. The contribution c_1 is varying
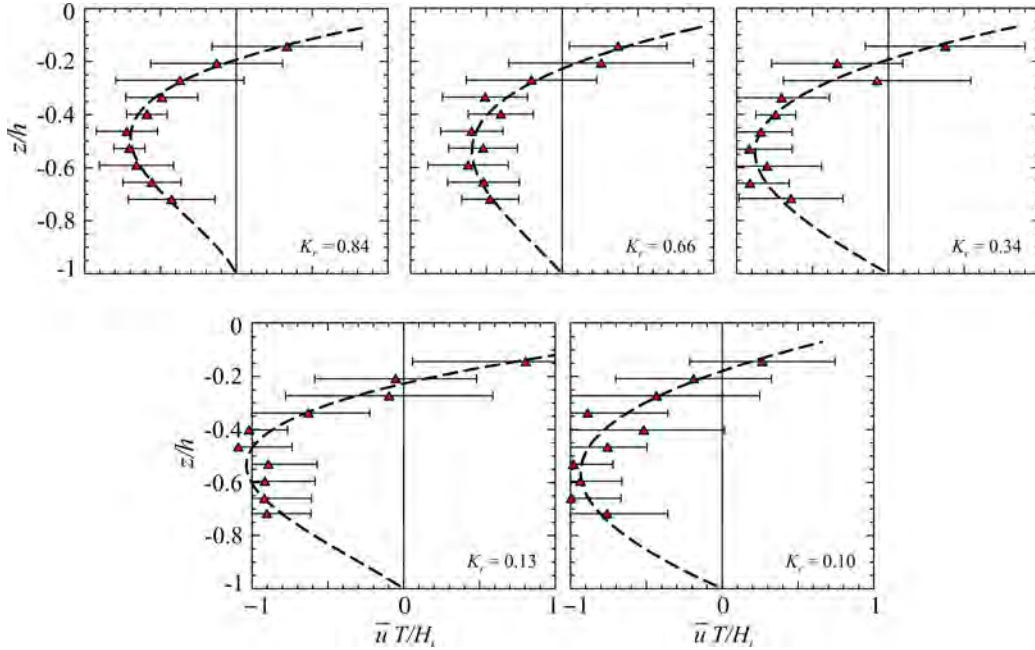
23

Figure 11: Experimental mean horizontal velocity measured with LDV in section of US2 where $x = -0.95$ m, with a fetch of 9.25 m. Symbols are the experiments, the dashed curves are the interpolating third order polynomials. Error bars are one standard deviation.

according to the profile of the current and the characteristics of the wave. Figure 11 shows experimental horizontal velocity measured with the LDV in Section 2 and the interpolating polynomials, where a no-slip condition is imposed at the bottom. We notice that mass balance is apparently not guaranteed, with a negative average mass flux for all experiments; hence, mass balance requires a three-dimensional pattern of the average flow field, with current profiles different near the lateral walls of the flume with respect to the profiles measured in the mid-section. This gives an indications of the approximations due to the laboratory effects, with currents in a finite size channel generally different from the currents in the field. See also the description of the average flow field in the presence of only wind in Longo et al. (2012).

The experimental phase celerity is calculated through the cross-correlation of the signals of two adjacent US sensors, after checking a good coherence (not shown) between signals using the cross-spectral function (see Newland, 2012).

Section	x (m)	c ($\mathrm{m\,s^{-1}}$)	f_{peak} ($\mathrm{s^{-1}}$)	k_{peak} ($\mathrm{m^{-1}}$)	c_g ($\mathrm{m\,s^{-1}}$)
US2	-0.94	-	-	-	-
		0.90 ± 0.03	1.91	14.6 ± 0.8	0.69 ± 0.04
US3	-0.79	0.87 ± 0.03			
		0.85 ± 0.03	1.94	15.1 ± 1.1	0.64 ± 0.01
US4	-0.65	0.87 ± 0.03			
		0.89 ± 0.01	1.89	14.4 ± 0.9	0.67 ± 0.04
US5	-0.49	0.91 ± 0.03			
		0.93 ± 0.02	1.84	13.6 ± 0.7	0.72 ± 0.02
US6	-0.33	0.92 ± 0.03			
		0.91 ± 0.03	1.87	14.0 ± 0.8	0.81 ± 0.03
US7	-0.16	0.89 ± 0.03			
		0.88 ± 0.01	1.86	13.9 ± 0.6	0.83 ± 0.03
US8	0	-	-	-	-

Table 3: Time average phase and group celerities for WGW in Expt PoW1. x is the US probe measurement section, c is the phase celerity, f_{peak} is the peak of the spectrum of the WGW (after removal of the periodic component), $k_{peak} \equiv 2\pi f_{peak}/c$ is the WGW wave number, c_g is the time average group celerity.

The average phase celerity between two probes is computed as $c = \Delta x/\Delta \tau$, where Δx is the distance between the sensors, and $\Delta \tau$ is the time lag which gives the maximum cross-correlation.

The group celerity c_g, which indicates the speed of propagation of the wave energy packets, is evaluated experimentally on the basis of the delay of the maximum of the cross-correlation envelope (Newland, 2012; Longo, 2012). Table 3 lists the results for Expt 1.

Figure 12 shows the phase and group celerities as a function of the wave number k for different reflective conditions. The linear dispersion relation for the phase and the group celerities is represented with c_0 (solid line) and $c_{g,0}$ (dotted line), respectively. The highest values of celerity (and of wavelength) are in the troughs, the lower values are in the crests, with a more evident difference for low reflective conditions $K_r = 0.10$.

The linear dispersion relation always underestimates experimental values, while considering the non-linear influence of the current profile through the

model defined by Swan and James (2000) yields a better interpretation of the phase celerity computed considering the whole sample (without differentiating the celerity of the short waves in the crests, troughs, downwind and upwind sides), and fits the experiments within the experimental uncertainties for most cases (black stars). On the contrary, the celerities of the short waves discriminated according to their position with respect to the phase of the paddle wave, show significant differences with the theory even at low values of K_r. This is attributed to the wave induced horizontal velocity, which sums up to the current profile shown in Figure 11: for a progressive wave without reflection ($K_r = 0$), we expect that in the crest the horizontal velocity is reduced with respect to time average value, the opposite is true in the trough and no effect should be observed in the downwind and upwind sides; in the presence of reflection, the effects depend on the reflection coefficients and on the position of the probe with respect to the (quasi-)nodes-antinodes. Figure 13 shows the relative position of the nodes-antinodes, of the sections of the probes, and of the upper envelope of the horizontal velocity at $z = 0$. Hence, the theoretical values of the celerity have been corrected with the model by Swan and James (2000) by considering the phase resolved horizontal velocity profiles (considering also the position of the probes) plus the measured current profiles in Section 2.

A further correction has been applied by including the non-inertial effects acting on the wind waves riding the swell. The short waves propagate over the swell and, as a first simple assumption, are subject to a vertical acceleration negative (downward) in the crests, and positive (upward) in the troughs of the swell. The result is a reduction/increment of the body force, with a consequent reduction/increment of the celerity in the dispersion relation. This apparent acceleration has been considered for non-linear waves by Longuet-Higgins (1987) and has been considered a factor increasing the white-capping instability (Hasselmann, 1971).

Vertical acceleration profiles decay beneath the water level and change during the phases of the swell. For each phase, we assumed a unique value of the acceleration equal to the depth-average acceleration in the range $[0, L_w/2]$(where L_w is the WGW wave length), with a further time-average in an interval $T/4$ across the phase. Table 4 lists the computed vertical acceleration for Exp. PoW1, with values dimensionless with respect to gravity acceleration. Peak values up to 20% of g result in Section 4, where the quasi-antinode is located. The acceleration is null in the downwind/upwind phases, but is quite relevant for crests/troughs in many sections of measure-

ment. The results for the other tests are similar, although the acceleration slightly decreases for decreasing reflection coefficient.

Figure 14 shows the comparison between the experimental and the theoretical celerity with the three different models. Figure 14a reports theoretical celerities computed by adopting Swan and James model and considering only the horizontal current measured in Section 2, where the LDV was installed. The theory systematically underestimates the experimental values, mainly in the troughs and for low reflection coefficients. Figure 14b reports theoretical celerities computed by adopting again the Swan and James model and considering current plus the orbital wave-induced horizontal velocity, with a better agreement with experimental celerity. Figure 14c reports theoretical celerities computed by adopting again the Swan and James model with current and the orbital wave-induced horizontal velocity, plus the correction for the vertical acceleration due to the swell. A further improvement can be observed, with an average underestimation equal to $\approx 25\%$. The Pearson correlation coefficient and the root mean square error (ρ and RMSE, respectively) also indicate the progressive improvement considering only current, current and orbital velocity, current, orbital velocity and vertical acceleration (from panel 14a to panel 14c). There are still some deviations of theory from the experiments, with the former systematically underestimating the latter. The discrepancies are attributable to some properties of shorter waves not included in the model, first of all their three dimensional nature with short crests and with an increased celerity (see, e.g. Wei et al., 2017). It is a matter of evidence that in the present experiments faster WGWs, which have presumably reached a quasi-2D structure, are better predicted than slower WGWs. There is also a vertical vorticity field due to short-crested wave breaking which is continuously injected in the flow field, and a circulation inside the wave flume with a three dimensional structure affecting the short waves kinematics. We should also consider the complexity of the present experiments scenario with respect to the scheme of the Swan and James model, and the non-homogeneity of the gravitational field within the non-inertial system of reference attached to the MGW. In summary, while the corrections are in the right direction, they are still not comprehensive of the numerous phenomena intervened in modifying the model.

Section	1	2	3	4	5	6	7	8
crest	-0.06	-0.17	-0.18	-0.19	-0.18	-0.15	-0.11	-0.06
downwind	0.00	0.00	0.00	0.00	0.00	0.00	0.00	0.00
trough	0.06	0.17	0.18	0.19	0.18	0.15	0.11	0.06
upwind	0.00	0.00	0.00	0.00	0.00	0.00	0.00	0.00

Table 4: Average vertical acceleration due to the swell dynamics non dimensional with respect to g, for Exp. PoW1.
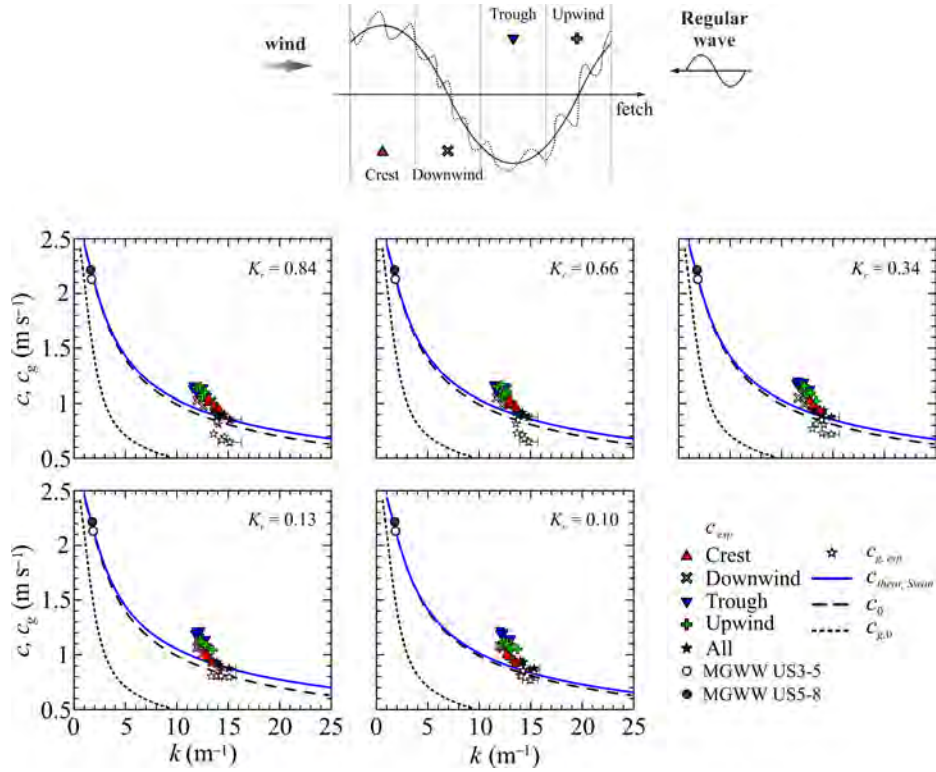

Figure 12: Phase and group celerities of WGW in the presence of MGW and different reflective conditions. Linear theory phase celerity (solid line) and theoretical group celerity (dashed line), and experimental values (symbols), as a function of the WGW wave number k. The blue dash-dotted line represents the phase celerity derived by Swan and James (2000). The error bars are one standard deviation.
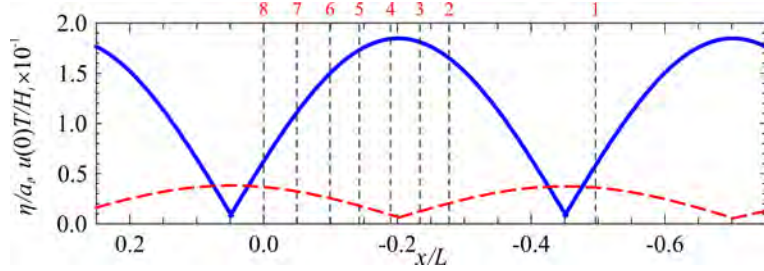
Figure 13: Upper envelopes of water level η/a_i (continuous curve) and horizontal velocity at $z = 0$, $u(0)T/H_t$ (dashed curve) for Exp. PoW1, $K_r = 0.843$. The vertical dashed line are the sections of measurements.
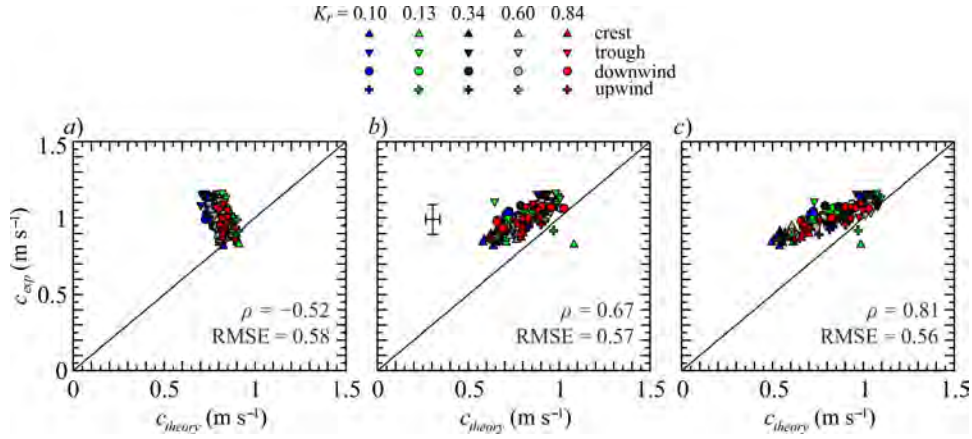

Figure 14: Comparison between experimental and theoretical phase celerity. *a*) Theoretical celerity based on Swan and James (2000) model considering the measured horizontal current profile; *b*) theoretical celerity based on Swan and James (2000) model considering the measured horizontal current profile and the horizontal wave-induced velocity; *c*) as in *b*) with a further correction due to the vertical acceleration. ρ and RMSE represent the Pearson correlation coefficient and the root mean square error, respectively. Results are discriminated for each phase.

6. Conclusions

We conducted an experimental study on MGW and opposing WGW interaction. The spectral filter technique chosen to separate the periodic MGW and the WGW components, guarantees a fairly good overlap between experiments and theory for several variables, and can be considered an adequate tool for processing data with mixed wind-waves and swell.

For the MGW, we adopt the theoretical model developed in Addona et al. (2018), which shows good agreement for the total wave height and the mean water level in the measured domain, although for longer fetch some discrepancy can arise if wind-induced dissipation is not taken into account. The observed effect of a wind blowing against the swell is a reduction of the wave height, which is consistent with the wave attenuation found in literature (see Peirson et al., 2003). The results also show novel aspects of the WGW interactions, in particular a reduction of the reflection coefficient and a reduction of the phase shift between incident and reflected waves, which is novel and is not quantitatively interpretable as due to energy dissipation generated by the wind.

The general behaviour of the WGW height is an initial growth due to the supply of wind energy, followed by an attenuation due to possible micro-breaking and non-linear transfer to longer waves. The peak period of WGW increases monotonically for increasing fetch length, while the wave steepness shows a variegate spatial evolution. The effects of reflective conditions are evident for two of the three quantities: (i) we notice that increasing reflective conditions yields a reduction of the wave height, which suggests a reduced efficiency in the transfer of WGW energy or a greater non-linear transfer of energy; (ii) the WGW period is almost unvaried with reflection; (iii) the wave steepness is generally minor for increasing reflection coefficient.

Further analysis has been conducted by separating WGW according to their position with respect to the phase of the MGW. As a first approach, WGW propagate on the wavy shape of the MGW with interactions in a linear fashion, and we expect different characteristics of the WGW in the crest and in the trough of the MGW, as well as leeward and windward from the crest. The phase-conditional analysis (phase is referred to the MGW) by considering four sub-domains for the WGW provided much more information about the WGW growth and the evolution with the fetch length of the WGW height, period and steepness. The additional insights that we found in our experiments are that:

- for increasing reflection, H_{rms} decreases on the downwind sides (much evident for the crests) as a result of the shielding, and increases on the upwind side;

- for increasing reflection, a higher growth rate of the mean period T_m in the downwind sides is observed, with the maximum in the crest, and a decay rate in the upwind side, with a minimum in the trough;

- for increasing reflection, the steepness kH_{rms} decreases with the length of the fetch on the downwind sides.

The WGW propagation along the flume is also studied by estimating the phase and group celerities. The effects of sheared horizontal currents are included through a perturbation model (Swan and James, 2000) which shows a good overlap with the experimental phase celerity if they are analysed en block. Phase-resolved celerities are better interpreted by including the wave-induced horizontal velocity in each phase, with varying effects also according to the spatial position of the section of measurement. A further correction includes the apparent vertical acceleration of the non-inertial frame of reference (the MGW) of the WGW: it is an apparent body force summing or subtracting to gravity in the troughs and in the crests, respectively, modifying the results of the dispersion relation. The overall results guarantees a stronger coherence between theory and experiments, although some differences are still noticeable. Further ad hoc experiments are requested, in order to shed light on these aspects, all relevant for improving conceptual models and for increasing the accuracy of numerical models.

References

Addona, F., 2019. Swell and wind-waves interaction under partial reflection conditions. Ph.D. thesis, Università di Parma - Universidad de Granada.

Addona, F., Loarca, A. L., Chiapponi, L., Losada, M. A., Longo, S., 2018. The Reynolds wave shear stress in partially reflected waves. Coastal Engineering 138, 220–226.

Baquerizo, A., 1995. Reflexión del oleaje en playas. Métodos de evaluación y de predicción. Ph.D. thesis, Universidad de Cantabria, Santander.

Belcher, S. E., Harris, J. A., Street, R. L., 1994. Linear dynamics of wind waves in coupled turbulent air—water flow. Part 1. Theory. Journal of Fluid Mechanics 271, 119–151.

Bitner-Gregersen, E., Toffoli, A., 2014. Occurrence of rogue sea states and consequences for marine structures. Ocean Dynamics 64 (10), 1457–1468.

Bredmose, H., Bullock, G. N., Hogg, A. J., 2015. Violent breaking wave impacts. Part 3. Effects of scale and aeration. Journal of Fluid Mechanics 765, 82–113.

Buckley, M. P., Veron, F., 2019. The turbulent airflow over wind generated surface waves. European Journal of Mechanics-B/Fluids 73, 132–143.

Chen, G., Belcher, S. E., 2000. Effects of long waves on wind-generated waves. Journal of Physical Oceanography 30 (9), 2246–2256.

Chiapponi, L., Addona, F., Diaz-Carrasco, P., Losada, A. M., Longo, S., 2020. Statistical analysis of the interaction between wind-waves and currents during early wave generation. Coastal Engineering 159, 103672.

Clavero, M., Longo, S., Chiapponi, L., Losada, M. A., 2016. 3D flow measurements in regular breaking waves past a fixed submerged bar on an impermeable plane slope. Journal of Fluid Mechanics 802, 490–527.

Cobos, M., Chiapponi, L., Longo, S., Baquerizo, A., Losada, M. A., 2017. Ripple and sandbar dynamics under mid-reflecting conditions with a porous vertical breakwater. Coastal Engineering 125, 95–118.

Feddersen, F., Veron, F., 2005. Wind effects on shoaling wave shape. Journal of Physical Oceanography 35 (7), 1223–1228.

Hasselmann, K., 1971. On the mass and momentum transfer between short gravity waves and larger-scale motions. Journal of Fluid Mechanics 50 (1), 189–205.

Hughes, S. A., 1993. Physical models and laboratory techniques in coastal engineering. Vol. 7. World Scientific.

Longo, S., 2003. Turbulence under spilling breakers using discrete wavelets. Experiments in Fluids 34 (2), 181–191.

Longo, S., 2012. Wind-generated water waves in a wind tunnel: Free surface statistics, wind friction and mean air flow properties. Coastal Engineering 61, 27–41.

Longo, S., Liang, D., Chiapponi, L., Jiménez, L. A., 2012. Turbulent flow structure in experimental laboratory wind-generated gravity waves. Coastal Engineering 64, 1–15.

Longuet-Higgins, M. S., 1987. The propagation of short surface waves on longer gravity waves. Journal of Fluid Mechanics 177, 293–306.

Longuet-Higgins, M. S., Stewart, R. W., 1960. Changes in the form of short gravity waves on long waves and tidal currents. Journal of Fluid Mechanics 8 (4), 565–583.

Lykke-Andersen, T., Clavero, M., Frigaard, P., M., L., Puyol, J. I., 2016. A new active absorption system and its performance to linear and non-linear waves. Coastal Engineering 114, 47–60.

Mansard, E. P. D., Funke, E. R., 1980. The measurement of incident and reflected spectra using a least squares method. In: Proc. 17th Coastal Engrg. Conf. Vol. 1. American Society of Civil Engineers, pp. 154–172.

Massey, B. S., 1971. Units, Dimensional Analysis and Physical Similarity. Van Nostrand Reinhold Company, London.

Newland, D. E., 2012. An introduction to random vibrations, spectral & wavelet analysis. Courier Corporation.

Olfateh, M., Ware, P., Callaghan, D. P., Nielsen, P., Baldock, T. E., 2017. Momentum transfer under laboratory wind waves. Coastal Engineering 121, 255–264.

Peirson, W. L., Garcia, A. W., Pells, S. E., 2003. Water wave attenuation due to opposing wind. Journal of Fluid Mechanics 487, 345–365.

Peregrine, D. H., 2003. Water-wave impact on walls. Annual Review of Fluid Mechanics 35 (1), 23–43.

Phillips, O. M., 1963. On the attenuation of long gravity waves by short breaking waves. Journal of Fluid Mechanics 16 (3), 321–332.

Stewart, R. H., Teague, C., 1980. Dekameter radar observations of ocean wave growth and decay. Journal of Physical Oceanography 10 (1), 128–143.

Swan, C., James, R. L., 2000. A simple analytical model for surface water waves on a depth-varying current. Applied Ocean Research 22 (6), 331–347.

Teixeira, M. A. C., Belcher, S. E., 2006. On the initiation of surface waves by turbulent shear flow. Dynamics of Atmospheres and Oceans 41 (1), 1–27.

Toba, Y., 1988. Similarity laws of the wind wave and the coupling process of the air and water turbulent boundary layers. Fluid Dynamics Research 2 (4), 263.

Toffoli, A., Bitner-Gregersen, E., Osborne, A., Serio, M., Monbaliu, J., Onorato, M., 2011. Extreme waves in random crossing seas: Laboratory experiments and numerical simulations. Geophysical Research Letters 38 (6).

Toffoli, A., Lefevre, J., Bitner-Gregersen, E., Monbaliu, J., 2005. Towards the identification of warning criteria: analysis of a ship accident database. Applied Ocean Research 27 (6), 281–291.

Toffoli, A., Onorato, M., Bitner-Gregersen, E., Osborne, A., Babanin, A., 2008. Surface gravity waves from direct numerical simulations of the euler equations: a comparison with second-order theory. Ocean Engineering 35 (3-4), 367–379.

Unna, P. J. H., 1947. Sea waves. Nature 159 (4033), 239–242.

Wei, Z., Dalrymple, R. A., Xu, M., Garnier, R., Derakhti, M., 2017. Short-crested waves in the surf zone. Journal of Geophysical Research: Oceans 122 (5), 4143–4162.